The solubility of monazite ($LaPO_4$, $PrPO_4$, $NdPO_4$, and $EuPO_4$) endmembers in aqueous solutions from 100 to 250 °C

Christopher J. Van Hoozen[a], Alexander P. Gysi[a,b,c] *, Daniel Harlov[d,e,f]

[a] Center for Mineral Resources Science, Department of Geology and Geological Engineering, Colorado School of Mines, Golden, CO 80401, USA

[b] Department of Earth and Environmental Science, New Mexico Institute of Mining and Technology, Socorro, NM 87801, USA

[c] New Mexico Bureau of Geology and Mineral Resources, New Mexico Institute of Mining and Technology, Socorro, NM 87801, USA

[d] GeoforschungsZentrum, Telegrafenberg, D-14473 Potsdam, Germany

[e] State Key Laboratory of Geological Processes and Mineral Resources, China University of Geosciences, Wuhan 430074, China

[f] Department of Geology, University of Johannesburg P.O. Box 524, Auckland Park, 2006

* Corresponding author: agysi@mines.edu

Tel: +1 303 273 3828

Revision 1 submitted to

Geochimica et Cosmochimica Acta

ABSTRACT

Monazite is a light rare earth element (REE) phosphate found in REE mineral deposits, such as those formed in (per)alkaline and carbonatite magmatic-hydrothermal systems, where it occurs in association to the development of alteration zones and hydrothermal veins. Although it has been recognized that monazite may undergo replacement by coupled dissolution-precipitation processes, currently there is no model describing the compositional REE variations in monazite resulting from direct interaction with or precipitation from hydrothermal fluids. To develop such a model requires quantification of the thermodynamic properties of the aqueous REE species and the properties of the monazite endmembers and their solid solutions. The thermodynamic properties of monazite endmembers have been determined previously using calorimetric methods and low temperature solubility studies, but only a few solubility studies have been conducted at > 100 °C. In this study, the solubility products ($\log K_{s0}$) of $LaPO_4$, $PrPO_4$, $NdPO_4$, and $EuPO_4$ monazite endmembers have been measured at temperatures between 100 and 250 °C and saturated water vapor pressure. The solubility products are reported with an uncertainty of ±0.2 (95% confidence) according to the reaction, $REEPO_4(s) = REE^{3+} + PO_4^{3-}$.

t (°C)	$\log K_{s0}$ ($LaPO_4$)	$\log K_{s0}$ ($PrPO_4$)	$\log K_{s0}$ ($NdPO_4$)	$\log K_{s0}$ ($EuPO_4$)
100	-28.0	-28.0	-28.1	-27.7
150	-28.8	-29.0	-29.0	-28.5
200	-30.2	-30.4	-30.6	-30.2
250	-32.1	-32.0	-32.3	-32.1

The REE phosphates display a retrograde solubility, with the measured K_{s0} values varying several orders of magnitude over the experimental temperature range.

Discrepancies were observed between the experimental solubility products and the calculated values resulting from combining calorimetric data of monazite with the properties of the aqueous REE^{3+} and PO_4^{3-} species available in the literature. The differences between the calculated and measured standard Gibbs energy of reaction ($\Delta_r G^0$) for $PrPO_4$, $NdPO_4$, and $EuPO_4$ increased with higher temperatures (up to 15 kJ mol^{-1} at 250 °C), whereas for $LaPO_4$ these differences increased at lower temperatures (up to 8 kJ mol^{-1} at 100 °C). To reconcile these discrepancies, the standard enthalpy of formation ($\Delta_f H^0$) of monazite was optimized by fitting the experimental solubility data and extrapolating these fits to reference conditions of 25 °C and 1 bar. The optimized thermodynamic data provide the first internally consistent dataset for the solubility of all the monazite endmembers, and can be used to model REE partitioning between monazite and hydrothermal fluids at > 100 °C.

1. INTRODUCTION

Monazite is a common accessory mineral, and has proven to be a useful geological tracer for geochronology and geothermometry in sedimentary, metamorphic, and igneous environments (Montel et al., 1996; Poitrasson et al., 1996; Gratz and Heinrich, 1997; Heinrich et al., 1997; Pyle et al., 2001; Farley and Stockli, 2002; Harrison et al., 2002; Spear and Pyle, 2002; Schaltegger et al., 2005; Rasmussen et al., 2011). The dominant REE phosphate endmember composition found in nature is monazite-(Ce), with the other light (L)REE (La, Pr, Nd, Sm, Eu, and Gd) preferentially incorporated over the smaller heavy (H)REE in its monoclinic ($P2_1/n$) structure (Ni et al., 1995). The stability of hydrothermal monazite can provide insights into the development of alteration zones in REE mineral deposits, such as in the giant Bayan Obo carbonatite deposit in China (Smith et al., 1999, 2000, 2016), the Browns Range vein deposit in Australia (Cook et al., 2013), and in metamorphic systems such as the Olserum-Djupedal in SE Sweden (Andersson et al., 2018a, 2018b). The stability of hydrated REE phosphates is also important in the formation of REE ion-adsorption deposits upon weathering and regolith development, such as those found in southern China and the southeastern United States (Foley et al., 2014; Xu et al., 2017; Li et al., 2019). In iron-oxide-apatite (IOA) deposits, such as Pea Ridge (Missouri, USA) and Kiruna (Sweden), monazite typically forms also as a hydrothermal phase associated with the replacement of apatite (Harlov et al., 2002, 2016). Experimental studies have confirmed the important role of aqueous fluids in the stability of REE phosphates and their control on the mobility of trace elements during crustal metasomatism (Ayers and Watson, 1991; Teufel and Heinrich, 1997; Seydoux-Guillaume et al., 2002; Poitrasson et al., 1996, 2004; Schmidt et al., 2007; Hetherington et al., 2010; Harlov et al. 2011; Tropper et al., 2011; Williams et al., 2011; Mair et al., 2017). Thus, determining the stability of monazite in hydrothermal fluids is paramount because its composition may be a useful tracer of fluid-rock interaction processes in these natural systems.

The thermodynamic properties of monazite endmembers have been determined from calorimetric measurements (Ushakov et al., 2001; Thiriet et al., 2005; Popa and Konings, 2006; Janots et al., 2007; Gavrichev et al., 2009, 2016; Thust et al., 2015; Bauer et al., 2016; Geisler et al., 2016; Hirsch et al., 2017; Neumeier et al., 2017). Several calorimetric, spectroscopic, and computational studies have recently shown that monazite displays non-ideal solid solution behavior, despite the similarity in ionic radii of the different REE (Popa et al., 2007; Li et al., 2014; Bauer et al., 2016; Geisler et al., 2016; Gysi et al., 2016; Hirsch et al., 2017; Huittinen et al., 2017; Neumeier et al., 2017). While data for the thermodynamic properties of most of these solids seem to be reliably known, the calculated versus the measured solubility of the REE phosphates in aqueous solution still displays significant discrepancies (Pourtier et al., 2010; Gysi et al., 2015, 2018). This results from combining calorimetric data from these minerals with the available thermodynamic data of the REE aqueous species from different literature sources. The latter have been mostly estimated and/or extrapolated to higher temperatures from low temperature data (Haas et al., 1995), except for the REE chloride, sulfate, and fluoride complexes (Migdisov et al., 2009, 2016).

The solubility of REE phosphate hydrates (rhabdophane, $REEPO_4 \cdot 0.667H_2O$) has been determined in aqueous solutions at low temperatures (< 100 °C) for all the endmembers (Jonasson et al., 1985; Firsching and Brune, 1991; Byrne and Kim, 1993; Firsching and Kell, 1993; Liu and Byrne, 1997; Poitrasson et al., 2004; Cetiner et al., 2005; Gausse et al., 2016; Shelyug et al., 2018). However, only a handful of monazite solubility experiments have been conducted in aqueous solutions at temperatures > 100 °C (Poitrasson et al., 2004; Cetiner et al., 2005; Pourtier et al., 2010; Gysi et al., 2018). Here we present experimental solubility data for the monazite $LaPO_4$, $PrPO_4$, $NdPO_4$, and $EuPO_4$ endmembers over a temperature range of 100 to 250 °C and saturated water vapor pressure (*swvp*). This work is part of a series of experimental solubility studies aimed at constructing a comprehensive internally consistent dataset for the REE phosphates and REE aqueous species (Gysi et al., 2015, 2018). Comparison of the measured monazite solubility with previously reported thermodynamic properties for REE phosphates and REE aqueous species are used to reconcile the inconsistencies resulting from a combination of different sources of data. The experimental data are then extrapolated to reference conditions of 1 bar and 25 °C, and we provide recommended thermodynamic data for modeling the solubility of REE phosphates in hydrothermal fluids.

2.1. MATERIALS

Individual mm-sized $LaPO_4$, $PrPO_4$, $NdPO_4$, and $EuPO_4$ crystals of monazite were grown from a Na_2CO_3-MoO_3 melt flux utilizing the synthetic method outlined in Cherniak et al. (2004). This synthesis method yields high-purity euhedral monoclinic monazite crystals (99.97 – 99.99%; Electronic Annex). The use of single crystals in solubility studies presents advantages over the use of poorly crystalline fine-grained mineral powders, which is discussed in more detail in the solubility study by Gysi et al. (2018). For the synthesis of these crystals, REE phosphate hydrates were precipitated from solution by mixing aqueous $REE(NO_3)_3$ and $NH_4H_2PO_4$. The resulting precipitates were dried and dry-mixed with a Pb-free Na_2CO_3-MoO_3 mixture ($75Na_2CO_3$:$25MoO_3$:$REEPO_4$). This mixture was then heated in a Pt crucible to 1375 °C over 4 hours and then allowed to 'soak' for 15 hours. The now molten flux was then subsequently cooled from 1375 °C to 870 °C at a rate of 3 °C/hour over a period of approximately 5 days. The Pt crucible was then removed from the oven and air-cooled. The Pt crucible, with the solidified flux plus embedded crystals, was then placed in successive beakers of boiling distilled H_2O until the crystals were freed from the flux material, the cloudy dissolved flux poured off, and the H_2O completely clear.

The experimental starting solutions utilized in the solubility experiments were prepared using trace metal grade perchloric ($HClO_4$) and phosphoric (H_3PO_4) acid (Fisher Scientific). Concentrated perchloric acid was added dropwise to 400 ml of milli-Q filtered water (18 MΩ-cm) until a pH of 2.00 ±0.02 was measured at ambient temperature (22 ±2 ℃). These pH measurements were used to determine the perchloric acid concentration in the starting solutions. Perchloric acid was used to buffer the pH of the experimental solution because ClO_4^- does not readily form complexes with REE cations in aqueous solutions (Migdisov et al., 2016). A pH of 2.0 was selected to limit the formation of REE hydroxyl complexes and to increase the dissolution of the REE phosphate crystals. Then a 200 µl aliquot of 0.045 m phosphoric acid was added to the 400 ml perchloric acid solution to fix the minimum phosphate concentration in the experimental solution and to reduce the uncertainty in the measurement of P concentrations using inductively coupled plasma mass spectrometry (ICP-MS) analysis. Sample holders utilized in the solubility experiments were hand-made from annealed Ti foil (99.7 % metal basis, Alfa Aesar).

2.2. ANALYTICAL

The pH of the starting experimental solutions was measured at room temperature using a Metrohm unitrode with an integrated Pt1000 temperature sensor (model 6.0260.010) and a Metrohm 913 pH meter (precision of ±0.003 pH units and resolution of 0.001 pH units). The electrode was calibrated using commercial buffer solutions (Fisher Scientific; pH 2.00, 4.00, and 7.00; accuracy of ±0.01); pH-temperature compensated reading for the buffer solutions are considered by the built-in temperature sensor of the electrode to measure deviations from 25 °C. The ionic strengths of the experimental starting solutions (0.01 m) and the buffer solutions used for pH calibration (0.05 m) are relatively dilute; minor deviations are expected in the measured pH as a result of variations in liquid junction potentials. The estimated accuracy of pH measurements for the perchloric acid buffered starting experimental solutions is within ±0.03 pH units.

Dissolved REE and P concentrations were measured in the reacted experimental solutions (Appendix A) using a Perkin Elmer NexION quadrupole inductively coupled plasma-mass-spectrometer (ICP-MS). Samples and standards were all diluted using 2% nitric acid (Fisher Scientific, trace metal grade) blank solutions and were mixed in-line with an In internal standard (SCP Science, NIST traceable certified standard) to correct for instrumental drift. Calibration was carried out using multi-element REE and P standards, and individual La and Ce standards (SCP Science, NIST traceable certified standard). The individual REE standards of La and Ce were used to correct for interference from the formation of REE oxides ($REEO^{16}$) utilizing the method presented in Aries et al. (2000). Phosphorus is difficult to analyze in the lower ppb range (< 100 ppb) due to mass interference with the 2% nitric acid blank ($^{14}N^{16}OH$ and $^{15}N^{16}O$) resulting in high background counts. To avoid this problem, standard curves were created above 10 ppb, and the P concentration ranges of the diluted experimental solutions corresponded to values ranging between 100 and 800 ppb. The limit of detection (LOD) values determined from multiple analyses of the matrix-matched blank (3σ) were 11 ppb for P, 4 ppt for La, 2 ppt for Pr, 8 ppt for Nd, and 1 ppt for Eu. The analytical precision of triplicate ICP-MS runs based on a 95 % confidence level were < 3 % for P, and < 1 % for La, Pr, Nd, and Eu.

2.3. SOLUBILITY EXPERIMENTS

Solubility experiments were carried out in 45 ml teflon lined stainless steel batch reactors (4744, Parr Instruments) at 100, 150, 200, and 250 °C at *swvp*. Kinetic experiments were conducted throughout a period of 1 to 23 days at 100 °C to verify approach to equilibrium between the REE phosphate crystals and the aqueous solutions.

Experiments consisted of mounting mm-sized monazite crystals in hand-made Ti holders, which were then placed in 25 ml of the perchloric acid starting solution. The headspace was then purged with dry nitrogen gas for a period of 5 minutes upon which the reactors were sealed and placed into a furnace (Cole-Parmer, EW-33858-70). The temperature was maintained within 0.5 °C of the experimental setpoint and monitored using an Omega® temperature logger with a K-type thermocouple located at the center of the furnace. After completion of the experimental period, the reactors were removed and quenched in a cold water bath within 20 min. The recovered experimental solutions were diluted (1/6 per mass) with a 2% nitric acid (Fischer Scientific, trace metal grade) blank in preparation for REE and P analysis using solution ICP-MS. Empty Ti-holders and teflon vessels were then soaked in concentrated sulfuric acid solutions for approximately

48 h and then rinsed with milliQ water, followed by a 24 h soak in milliQ water before being utilized in new experiments. In-between experiments, a sulfuric acid wash was used to rinse the walls of the Teflon liner of the autoclaves. These solutions were further diluted with milliQ water and the REE were analyzed using ICP-MS to detect the formation of any potential precipitates upon quenching. These tests did not provide any evidence that quenching of the experiments led to the precipitation of additional REE solid phases in this type of experiment.

2.4. DATA TREATMENT

Speciation and activities of aqueous ions were calculated using the GEMS code package v.3.5 and the TSolMod library (Wagner et al., 2012; Kulik et al., 2013). Thermodynamic properties of the aqueous species were calculated using the revised HKF equation-of-state (Helgeson et al., 1981; Shock and Helgeson, 1988; Tanger and Helgeson, 1988; Shock et al., 1992). The properties of water were calculated from the IAPS-84 equations-of-state (Kestin et al., 1984). The thermodynamic data of the aqueous species considered in the speciation calculations are listed in Appendix C and were taken from Shock and Helgeson (1988), Shock et al. (1989, 1997), and Haas et al. (1995), which are collectively referred to as the Supcrt92 database.

The activities of the aqueous species of interest (REE^{3+}, $REEOH^{2+}$, H^+, $H_3PO_4^0$, $H_2PO_4^-$, HPO_4^{2-}, and PO_4^{3-}) were determined at the experimental temperatures and *swvp* using the measured concentrations of REE and P from the quenched experimental solutions, and the ClO_4^- concentrations obtained from the measured pH of the starting solutions (Appendix A). The activity coefficients (γ_i) of charged aqueous species were calculated using the extended Debye-Hückel equation (Robinson and Stokes, 1959) ,

$$\log\gamma_i = -\frac{A z_i^2\sqrt{I}}{1+åB\sqrt{I}} + \Gamma_\gamma + b_\gamma I \quad (1)$$

where the effective ionic strength *I*, is given by,

$$I = 1/2 \sum_i m_i z_i^2 \quad (2)$$

A and *B* are the Debye-Hückel parameters (Helgeson and Kirkham, 1974; Helgeson et al., 1981); *å* is the ion size parameter, which is 4.5 Å for ClO_4^-, and was selected from Kielland (1937) for the other ions; Γ_γ is a mole fraction to molality conversion factor; m_i and z_i are the molal concentration and charge number of the *i*th aqueous species, respectively; b_γ is the extended term parameter. The b_γ term is an empirical parameter that depends on the background electrolyte and has been experimentally determined for perchlorate-based ($HClO_4/NaClO_4$) aqueous solutions up to 250 °C as being equal to 0.21 (Migdisov and Williams-Jones, 2007).

The equilibrium constants for the dissolution of REE phosphate in aqueous solutions as a function of pH are described by the following set of reactions:

$REEPO_4(s) = REE^{3+} + PO_4^{3-}$ (K_{S0}) (3)

$REEPO_4(s) + H^+ = REE^{3+} + HPO_4^{2-}$ (K_{S1}) (4)

$REEPO_4(s) + 2H^+ = REE^{3+} + H_2PO_4^-$ (K_{S2}) (5)

$REEPO_4(s) + 3H^+ = REE^{3+} + H_3PO_4^0$ (K_{S3}) (6)

At a pH of 2.0, the dominant phosphate species in the experiments was $H_3PO_4^0$ and to a lesser extent $H_2PO_4^-$ (Appendix A). Therefore, K_{s3} was first determined at the experimental temperature using Reaction (6), with the equilibrium constant given by,

$$K_{s3} = \frac{a_{H_3PO_4^0} \times a_{REE^{3+}}}{a_{H^+}{}^3} \quad (7)$$

where a is the activity of $H_3PO_4^0$, REE^{3+}, and H^+, respectively. The deprotonation of orthophosphate can be described by,

$$H_3PO_4^0 = H^+ + H_2PO_4^- \ (K_1) \quad (8)$$

$$H_2PO_4^- = H^+ + HPO_4^{2-} \ (K_2) \quad (9)$$

$$HPO_4^{2-} = H^+ + PO_4^{3-} \ (K_3) \quad (10)$$

where K_1, K_2, and K_3 are the first, second, and third dissociation constants of phosphoric acid. The equilibrium constant of Reaction (3) can then be calculated by combining the dissociation constants of phosphoric acid (Reactions 8-10) with Eq. (7),

$$K_{s0} = K_{s3} \times K_1 \times K_2 \times K_3 \quad (11)$$

with the corresponding solubility product,

$$K_{s0} = a_{REE^{3+}} \times a_{PO_4^{3-}} \quad (12)$$

where a is the activity of REE^{3+} and PO_4^{3-}.

The source of thermodynamic data for Reactions (8-10) are listed in Appendix C. The dissociation constants of phosphoric acid were determined from standard thermodynamic properties and HKF parameters derived by Shock and Helgeson (1988), and Shock et al. (1989, 1997). These values are internally consistent and have been used to evaluate the speciation of phosphorous in our experiments. The predicted values of the first (K_1) and second (K_2) dissociation constants are consistent with the experimentally determined values by Mesmer and Baes (1974) using potentiometric measurements to 300 ºC. The accuracy of the first dissociation constant of phosphoric acid has also been confirmed by a recent Raman spectroscopy study by Rudolph (2012). The third (K_3)

dissociation constant could not be determined accurately at infinite dilution and above 150 °C by Mesmer and Baes (1974) and are based on predictions from the HKF correlations. The properties derived for the phosphate species from Shock and Helgeson (1988), and Shock et al. (1989, 1997), are therefore used in the present study because of their internally consistency and wide usage until further experimental data become available.

3. RESULTS

3.1. KINETIC EXPERIMENTS

To verify that equilibrium was approached within the experimental period, a series of kinetic runs was carried out over a period of 1 to 23 days at the lowest experimental temperature of 100 °C for $LaPO_4$ and $NdPO_4$ (Fig. 1). The solubilities of $LaPO_4$ and $NdPO_4$ were determined from the measured REE and P concentrations as a function of time (Appendix A), and the activities of REE^{3+} and PO_4^{3-} were calculated to determine the reaction quotient (Q_{s0}) according to Eq. (12). The results of the kinetic experiments indicate that the $\log Q_{s0}$ for $LaPO_4$ reached steady-state values of approximately -28.0 (±0.2 within a 95% confidence interval) after an experimental period of 14 days. The $\log Q_{s0}$ for $NdPO_4$ reached a steady-state value of -28.1 (±0.2 within a 95% confidence interval) after an experimental period of 5 days. These results suggest that equilibrium concentrations are approached in our experiments within a period of 5 to 14 days. These results are consistent with the solubility studies of Gysi et al. (2015, 2018), which employed the same experimental method, and found that the solubility of monazite and xenotime crystals reached steady-state concentrations after 10 days at 100 ºC, and after 5 days at 150 ºC.

3.2. SOLUBILITY PRODUCTS

The solubility products (K_{s0}) of $LaPO_4$, $NdPO_4$, $PrPO_4$, and $EuPO_4$ monazite crystals were determined from the measured REE and P concentrations of the quenched experimental solutions and the calculated aqueous species activities (Appendix A). The experimentally measured $\log K_{s0}$ values at infinite dilution as a function of temperature are reported in Table 1 and shown in Figure 2.

Replicate experiments display a standard deviations (1σ) of the reported mean $\log K_{s0}$ values ranging between ±0.01 and ±0.40 (Table 1). Based on error analysis of these replicate experiments, the uncertainty of the mean is estimated to be ±0.2 on the 95 % confidence interval. These uncertainties are in line with previous hydrothermal REE phosphate solubility experiments reporting an experimental reproducibility within or better than ±0.25 $\log K_{s0}$ units (Gysi et al., 2015, 2018). Possible uncertainties that can result from the accuracy of the pH measurements of the starting solutions were also evaluated. The initial perchloric acid concentrations of the experimental solutions were varied in GEMS to reach $pH_{25\,°C}$ values of 1.97, 2.00, and 2.03 (i.e., accuracy of pH measurements). The activities of REE^{3+} and PO_4^{3-} were then recalculated at the experimental temperatures and the resulting $\log K_{s0}$ values were determined between 100 and 250 ºC. This analysis yields $\log K_{s0}$ values within ±0.1–0.2 units at the higher and lower pH ends, respectively, in comparison to the values determined at a pH of 2.

All the REE phosphates display retrograde solubility and vary non-linearly between 100 and 250 ºC. The $\log K_{s0}$ values determined by this study vary four to five orders of magnitude within the experimental temperature range but yielded similar values between the different REE phosphate endemembers. The measured solubility products were fitted to an empirical non-linear fit of the following form,

$$\mathrm{logK} = \mathrm{A} + \mathrm{B} \times \mathrm{T} + \frac{\mathrm{C}}{\mathrm{T}} + \mathrm{Dlog(T)} \tag{13}$$

where T is the temperature in Kelvin. A, B, C, and D are the fitted coefficients, which are related to the standard enthalpy ($\Delta_r H^0_{Tr}$) and entropy ($\Delta_r S^0_{Tr}$) of reaction for the dissolution of monazite (Appendix D). In the experimental temperature range, only the first three terms of Eq. (13) could be retrieved for the initial fitting of the experimental data. The empirical fits and their prediction bound at 95 % confidence are displayed in Figure 2, and the fitted coefficients are listed in Table 2 (Fit 1) with regression coefficients (R^2) ranging between 0.986 and 0.996.

4. DISCUSSION

4.1. COMPARISON TO PREVIOUS STUDIES: SOLUBILITY OF MONAZITE AND RHABDOPHANE

Previous REE phosphate solubility studies were mostly conducted at ambient temperatures or below 100 °C (Jonasson et al., 1985; Firsching and Brune, 1991; Firsching and Kell, 1993; Byrne and Kim, 1993; Liu and Byrne, 1997; Cetiner et al., 2005; Gausse et al., 2016). The major difficulty in evaluating the solubility of REE phosphates stems from the formation of the metastable hydrated rhabdophane phase below 100 °C, which is more soluble than monazite (Du Fou de Kerdaniel et al., 2007; Gausse et al., 2016; Shelyug et al., 2018). This was recently confirmed in the kinetic study by Arinicheva et al. (2018). Other difficulties include the crystallinity of the solids used in the experiment such as powders versus larger crystals (Cetiner et al., 2005; Gysi et al., 2015, 2018). Hence most of the solubility data available below 100 °C seem to be controlled by the stability of rhabdophane. This was confirmed in the experiments by Gausse et al. (2016), who measured the solubility of rhabdophane between 25 and 90 °C, from both over- and undersaturation. Comparison of our measured monazite solubilities between 100 and 250 °C with previous experiments carried out at lower temperatures (Fig. 3) reveals systematically lower $\log K_{s0}$ values for monazite. Similar observations were made in a recent solubility study for $CePO_4$, $SmPO_4$, and $GdPO_4$ monazite endmembers measured between 100 and 250 °C by Gysi et al. (2018). Other monazite solubility studies conducted above 100 °C are scarce. Cetiner et al. (2005) and Poitrasson et al. (2004) measured the solubility of $NdPO_4$ monazite powders at 150 to 300 °C. The study of Poitrasson et al. (2004) shows excellent agreement with our solubility data at 200 and 300 °C, whereas the monazite data of Cetiner et al. (2005) displays an overall lower solubility than measured in our experiments at 150 °C (Fig. 3c).

In addition to the measured solubilities, solubility curves were calculated (Fig. 3) by combining the available calorimetric data for $LaPO_4$, $PrPO_4$, $NdPO_4$, and $EuPO_4$ (Table 3) with the thermodynamic properties of the REE^{3+} and PO_4^{3-} ions from the Supcrt92 database (Appendix C). The calculated solubility curves for $NdPO_4$ and $EuPO_4$ are consistently an order of magnitude lower than our experimental measurements (Fig.

3c-d). In contrast, the calculated solubility curves for $LaPO_4$ and $PrPO_4$ partly overlap with our experimental data and the measured solubilities for rhabdophane (Fig. 3a-b). The source of these discrepancies can result from the incompatibility of combining the thermodynamic properties of the minerals and aqueous species from different sources, whereas in the solubility experiments, the solubility products are solely calculated based on the speciation and activities of aqueous species and measured REE and P concentrations of the experiments.

The differences between the measured and calculated solubilities were further evaluated by constructing residual plots of the standard Gibbs energy of reaction (Δ_rG^0). The latter was retrieved from the measured solubilities according to,

$$\log K = \frac{-\Delta rG^0}{RT\ln(10)} \quad (14)$$

where R is the ideal gas constant and T is the temperature in K. Residual plots (Fig. 4) show that these discrepancies are generally larger with increasing temperatures for $PrPO_4$, $NdPO_4$, and $EuPO_4$, with negative residuals for Δ_rG^0 indicating higher measured solubilities in comparison to the calculated ones. In contrast, $LaPO_4$ shows higher discrepancies with decreasing temperatures, with positive residuals for Δ_rG^0 indicating lower measured solubilities in comparison to the calculated ones.

4.2. EXTRAPOLATION OF THE SOLUBILITY PRODUCTS TO REFERENCE CONDITIONS

Using the measured REE phosphate solubility products between 100 and 250 °C, it is desirable to extrapolate the empirical fits to reference conditions of 25 °C (T_r) and 1 bar

(P_r). Using a three-coefficients empirical fit (Fit 1, Table 3) would lead to large 95 % prediction intervals for extrapolated values at 25 °C. However, these fits can be improved by using the relationship between the fitted empirical coefficients A-D (Eq. 13) and the standard enthalpy ($\Delta_r H^0_{Tr,Pr}$) or the standard entropy ($\Delta_r S^0_{Tr,Pr}$) of reaction (Appendix D). This method utilizes the data available from the calorimetric measurements of the monazite endmembers to constrain a four-coefficient fit through the experimental data (Gysi et al., 2015, 2018). This optimization procedure consists of retrieving a four coefficient fit by either fixing $\Delta_r H^0_{Tr,Pr}$ and retrieving a value for $\Delta_r S^0_{Tr,Pr}$ (Fit 2, standard enthalpy of formation, $\Delta_f H^0_{Tr,Pr}$, of monazite optimized) or vice versa (Fit 3, absolute entropy, $S^0_{Tr,Pr}$, of monazite optimized). The results of this optimization technique and the fitted coefficients are listed in Table 2.

In the first optimization method (Fit 2, Table 2), the $\Delta_f H^0_{Tr,Pr}$ values derived by Ushakov et al. (2001) from high temperature oxide melt solution calorimetry of the monazite endmembers were used in combination with the data from Supcrt92 for REE^{3+} and PO_4^{3-} (Appendix C) to calculate and fix $\Delta_r H^0_{Tr,Pr}$ and coefficient D from Eq. (13). The fitted coefficient A was used to retrieve $\Delta_r S^0_{Tr,Pr}$, and was then used to solve for a new $S^0_{Tr,Pr}$ value for monazite. Comparison of the new optimized $S^0_{Tr,Pr}$ value with calorimetric measurements (Thiriet et al., 2005; Popa et al., 2006; Gavrichev et al., 2009, 2016) indicates that this optimization results in poor agreement with the measured calorimetric data for monazite. The relative entropy values differ by 5 to 30 J mol^{-1} K^{-1} in comparison to the reported values from the calorimetric studies (Table 2).

In the second optimization method (Fit 3, Table 2), the $S^0_{Tr,Pr}$ values of monazite, derived by Thiriet et al. (2005), Popa et al. (2006), and Gavrichev et al. (2009, 2016) from low temperature adiabatic relaxation calorimetry, were used to calculate $\Delta_r S^0_{Tr,Pr}$ and fix coefficient A during the fitting procedure (Eq. 3). The coefficient D was then retrieved from the fit and related to the $\Delta_r H^0_{Tr,Pr}$ (Appendix D), which was then used to solve for a new $\Delta_f H^0_{Tr,Pr}$ value for monazite. The agreement between these new $\Delta_f H^0_{Tr,Pr}$ values, retrieved from the fits of the solubility data and the measured calorimetric enthalpies (Ushakov et al., 2001; Janots et al., 2007; Hirsch et al., 2017; Neumeier et al., 2017), was used to evaluate the quality of these fits (Table 2). The new $\Delta_f H^0_{Tr,Pr}$ values, determined for $PrPO_4$, $NdPO_4$, and $EuPO_4$ from the solubility experiments, display an excellent agreement with the calorimetric studies, and range within 3 kJ mol^{-1} of the values reported by Ushakov et al. (2001). In contrast, the $\Delta_f H^0_{Tr,Pr}$ value obtained from the solubility experiments for $LaPO_4$ (-1980.5 kJ mol^{-1}) is 10 kJ mol^{-1} more negative than the value reported by Ushakov et al. (2001), but is within the range of other reported enthalpy values (Janots et al., 2007; Hirsch et al., 2017; Neumeier et al., 2017). The agreement between this optimization and the calorimetric $\Delta_f H^0_{Tr,Pr}$ data for monazite suggests that Fit 3 is the most accurate for extrapolating our data to reference conditions.

To test whether Fit 3 (Table 2) can be used to reconcile the discrepancies observed between the calorimetric data of monazite combined with the aqueous species of the Supcrt92 database, these $\log K_{s0}$ values were recalculated between 100 and 250 °C with the newly optimized $\Delta_f H^0_{Tr,Pr}$ values. As shown in Figure 5, discrepancies are still observed between the measured solubility products and the optimized values, especially with increasing temperatures. Calculated residuals (Fig. 4) indicate that the fits are mostly improved for $NdPO_4$ and $EuPO_4$ but not for $LaPO_4$ and $PrPO_4$. These observations suggest that some of the observed discrepancies result from the REE aqueous species.

The thermodynamic properties of the REE aqueous species from Supcrt92 derived by Haas et al. (1995) may need to be reevaluated, which has been corroborated by numerous previous experimental studies (Migdisov et al., 2009, 2016). The observed discrepancies between the measured solubilities and the combination of different sources of thermodynamic data for the minerals and aqueous species can result from the calculated activities of the REE^{3+} ion and additional REE hydroxyl complexes such as $REEOH^{2+}$; the latter is predicted to become important with increasing temperatures of the experiments (Appendix A). Similar conclusions were made in the recent $CePO_4$, $SmPO_4$, and $GdPO_4$ solubility study by Gysi et al. (2018), who showed a possible optimization method for the REE aqueous species. Additional potentiometric studies may aid in better recognizing which aqueous REE hydroxyl species need revision. Nonetheless, we can currently recommend an optimized set of enthalpy data for monazite from our solubility study, which is presented in Table 3, and which already yields an improvement in the calculated solubilities of monazite in hydrothermal fluids.

4.3 MODELING THE SOLUBILITY OF MONAZITE IN HYDROTHERMAL FLUIDS

Here we demonstrate an application of our experimental data by modeling the partitioning of REE between an ideal monazite solid solution and an acidic hydrothermal fluid (pH of 2) reacted with 1 g leucogranite per kg H_2O. This model simulates the varying REE composition of monazite in a hydrothermal quartz-muscovite vein as a function of temperature from 25 to 300 ºC. Two different fluid compositions were used to test the controls of aqueous speciation (NaCl-HCl-H_2O-fluid with REE chloride complexes) vs. solubility of the REE phosphates ($HClO_4$-H_2O-fluid with only REE^{3+} and hydroxyl complexes).

Geochemical modeling was carried out using the GEMS code software package (Kulik et al., 2013) and the MINES thermodynamic database (http://tdb.mines.edu). Thermodynamic data of aqueous REE chloride complexes were taken from Migdisov et al. (2009); REE^{3+} and REE hydroxyl complexes were taken from the Supcrt92 database (Haas et al., 1995). To evaluate the impact of the optimized dataset for monazite retrieved from the solubility experiments, two ideal solid solution monazite phases were set up comprising all the light REE monazite endmembers (i.e., $LaPO_4$ to $GdPO_4$). The first monazite solid solution utilized the newly optimized dataset from the present study combined with the data for $CePO_4$, $SmPO_4$, and $GdPO_4$ from Gysi et al. (2018), and the second solid solution utilized the previously available calorimetric data of monazite (Table 3).

Comparison of the simulated monazite solid solution composition using the optimized thermodynamic data from the solubility experiments and the previously available data, indicates a significant impact on the simulated monazite compositions (Fig. 6). Our new dataset results in an increased stability for $LaPO_4$, $CePO_4$, $PrPO_4$, and a decreased stability for $NdPO_4$, $SmPO_4$, $EuPO_4$, and $GdPO_4$. This results in a calculated monazite composition that is consistent with natural monazite that is mostly composed of

La, Ce, and Nd (Förster, 1998; Harlov et al., 2016). Although Pr is predicted to have a higher stability than Nd, Sm, Eu, and Gd, natural monazite tends to only have 1-5 wt.% Pr_2O_3, which may partly reflect the relative crustal abundances of the different REE that may also need to be considered in such model (McDonough and Sun, 1995).

The solubility products of the different REE phosphates derived in this study have relatively similar values for an isotherm (Table 1). However, slight differences can affect considerably the calculated REE composition of monazite and the aqueous fluids. This is reflected by the model were monazite is equilibrated with the $HClO_4$-H_2O-fluid. A decrease in temperature from 300 to 25 ºC led to a shift from a monazite composition with calculated X_{REE} approaching each other, towards a monazite composition with highly fractionated X_{REE} values (Figs. 6a,c). This shift in monazite composition is controlled by the relative solubilities of the different REE phosphate endmembers and approach/divergence from saturation with monazite. The retrograde solubility of monazite resulted therefore in an increased REE fractionation with decreasing temperatures.

Figure 7 shows the experimental $\log K_{s0}$ values as a function of temperature and ionic radii of the REE, making a comparison between $LaPO_4$, $PrPO_4$, $NdPO_4$, and $EuPO_4$ measured in our study, and the solubility data for $CePO_4$, $SmPO_4$, and $GdPO_4$ from the study of Gysi et al. (2018). The measured solubility products of the REE phosphate endmembers are relatively similar, but there is a noticeable increase in solubility products for the REE phosphates that have a smaller ionic radius and higher atomic number, such as Sm, Eu, and Gd over the La, Ce, Pr, and Nd. There are also noticeable anomalies in Eu and Ce solubilities depending on temperature, which should be further explored. The slight lower solubility of $CePO_4$ compared to neighboring REE elements, is consistent with Ce^{3+} being the dominant ion in natural monazite. When modeling the solubility of monazite it has to be considered that the $\log K_{s0}$ values and calculated REE phosphate solubilities will depend, on both, the contribution of the Gibbs energy of the aqueous species and monazite (Eq. 3 and Eq. 14). Therefore, similar $\log K_{s0}$ values between the different REE phosphate endmembers do not necessarily imply the same calculated solubilities for all of the REE in full equilibrium speciation calculations. This explains why the optimizations of the thermodynamic properties of monazite and/or the aqueous REE species, and the checking of their compatibility retrieved from the solubility experiments is so important for accurate speciation calculations.

An additional factor that affects the relative stability of the different monazite endmembers in the solid solution is the stability of REE aqueous complexes, which are controlled by the fluid chemistry and temperature. This is illustrated by the model were monazite is equilibrated with the NaCl-HCl-H_2O-fluid (Figs. 6b,d). Using the optimized data from this study, indicates that with increased temperature (> 250 °C), there is an overall increase in the middle REE content in monazite (Fig. 6b). This shift in monazite composition can be explained because the lower atomic number REE, such as La and Ce, tend to form stronger chloride complexes in the fluid in comparison to the middle REE, such as Gd and Eu (Migdisov et al., 2009), making them therefore more mobile.

5. CONCLUSION

We have measured the solubility of $LaPO_4$, $PrPO_4$, $NdPO_4$, and $EuPO_4$ in aqueous perchloric acid solutions at temperatures from 100 to 250 °C at *swvp*. The results demonstrate thatLREE phosphates display a retrograde solubility which decreases sharply with increasing temperature. Since the more soluble metastable rhabdophane phase controls the solubility of REE phosphates below 100 °C, additional thermodynamic constraints were needed to extrapolate the measured solubility products to 25 °C and 1 bar.

The combined available calorimetric data for monazite and the thermodynamic data for REE aqueous species from the Supcrt92 database (Shock and Helgeson, 1988; Shock et al., 1989, 1997; Haas et al., 1995) show significant discrepancies with the measured solubility products between 100 and 250 °C (Fig. 3). To reconcile these discrepancies, optimization of the enthalpy of formation of monazite ($\Delta_f H^0_{Tr,Pr}$) can be done while maintaining consistency with the calorimetric entropy data. While this method alleviates some of the observed discrepancies, the optimization analysis indicates a need to revise the thermodynamic properties of REE^{3+} and/or the $REEOH^{2+}$ species. The latter are currently based on the theoretical predictions of Haas et al. (1995), which have been used by the research community in the past decades but may be the source of the observed discrepancies at elevated temperatures. REE hydroxyl complexes are among the least studied complexes under hydrothermal conditions (Migdisov et al., 2016). Currently, the only reported stability constants above 100 °C were measured in the study of Wood et al. (2002) for Nd complexes. The stability of $NdOH^{2+}$, for example, was determined only at 250 and 290 °C, but more complete experimental datasets are needed to evaluate the stability of these species as a function of temperature.

With the addition of solubility data for monazite collected in this study, coupled with the data available from Gysi et al. (2018), a complete internally consistent thermodynamic dataset is now available for modeling all monazite endmembers in hydrothermal systems (Table 3). While major revision of the stability of REE species may still be needed, and solid solution properties still need to be quantified to interpret REE signatures in natural monazite, the dataset provided in this study have proven to be able to more reliably replicate the dominant REE compositional trends observed in natural monazite (Fig. 6). It is shown that additional factors, such as the relative stability of the REE complexes and the REE crustal abundance, may account for some of the compositional variations that can be observed in the simulated monazite. Recent studies have also shown that the monazite solid solutions display a non-ideal mixing behavior (Popa et al., 2007; Li et al., 2014; Bauer et al., 2016; Geisler et al., 2016; Gysi et al., 2016; Hirsch et al., 2017; Huittinen et al., 2017; Neumeier et al., 2017). Thus, experimental measurement of the excess properties of mixing, in addition to the stability of missing REE complexes at elevated temperature, will be the next step to producing a predictive solid solution model for monazite formation in hydrothermal systems.

ACKNOWLEDGMENTS

This project was supported by the National Science Foundation to APG (NSF grant EAR-1649656). We would like to thank K. Challis and J. Ranville for help on the ICP-MS analysis. We are also grateful for the constructive comments by A. Migdisov and two anonymous reviewers, and would like to thank Associate Editor R. H. Byrne for handling this manuscript.

REFERENCES

Andersson S. S., Wagner T., Jonsson E., Fusswinkel T., Leijd M. and Berg J. T. (2018a) Origin of the high-temperature Olserum-Djupedal REE-phosphate mineralisation, SE Sweden: A unique contact metamorphic-hydrothermal system. *Ore Geol. Rev.* **101**, 740–764.

Andersson S. S., Wagner T., Jonsson E. and Michallik R. M. (2018b) Mineralogy, paragenesis, and mineral chemistry of REEs in the Olserum-Djupedal REE-phosphate mineralization, SE Sweden. *Am. Mineral.* **103**, 125–142.

Aries S., Valladon M., Polvé M. and Dupré B. (2000) A routine method for oxide and hydroxide interference corrections in ICP-MS chemical analysis of environmental and geological samples. *Geostand. Newsl.* **24**, 19–31.

Arinicheva Y., Gausse C., Neumeier S., Brandt F., Rozov K., Szenknect S., Dacheux N., Bosbach D. and Deissmann G. (2018) Influence of temperature on the dissolution kinetics of synthetic $LaPO_4$-monazite in acidic media between 50 and 130 °C. *J. Nucl. Mater.* **509**, 488–495.

Ayers J. C. and Watson E. B. (1991) Solubility of apatite, monazite, zircon, and rutile in supercritical aqueous fluids with implications for subduction zone geochemistry. *Philos. Trans. R. Soc. London. Ser. A Phys. Eng. Sci.* **335**, 139–149.

Bauer J. D., Hirsch A., Bayarjargal L., Peters L., Roth G. and Winkler B. (2016) Schottky contribution to the heat capacity of monazite type (La, Pr)PO_4 from low temperature calorimetry and fluorescence measurements. *Chem. Phys. Lett.* **654**, 97–102.

Byrne R. H. and Kim K. H. (1993) Rare earth precipitation and coprecipitation behavior: The limiting role of PO_4^{3-} on dissolved rare earth concentrations in seawater. *Geochim. Cosmochim. Acta* **57**, 519–526.

Cetiner Z. S., Wood S. A. and Gammons C. H. (2005) The aqueous geochemistry of the rare earth elements. Part XIV. The solubility of rare earth element phosphates from 23 to 150 °C. *Chem. Geol.* **217**, 147–169.

Cherniak D. J., Pyle J. and Rakovan J. (2004) Synthesis of REE and Y phosphates by Pb-free flux methods and their utilization as standards for electron microprobe analysis and in design of monazite chemical U-Th-Pb dating protocol. *Am. Mineral.* **89**, 1533–1539.

Cook N. J., Ciobanu C. L., O'Rielly D., Wilson R., Das K. and Wade B. (2013) Mineral chemistry of Rare Earth Element (REE) mineralization, Browns Ranges, Western Australia. *Lithos* **172–173**, 192–213.

Du Fou de Kerdaniel E., Clavier N., Dacheux N., Terra O. and Podor R. (2007) Actinide solubility-controlling phases during the dissolution of phosphate ceramics. *J. Nucl. Mater.* **362**, 451–458.

Farley K. A. and Stockli D. F. (2002) (U-Th)/He dating of phosphates: Apatite, monazite, and xenotime. *Rev. Mineral. Geochemistry* **48**, 559–577.

Firsching F. H. and Brune S. N. (1991) Solubility product of the trivalent rare-earth phosphates. *J. Chem. Eng. Data* **1**, 93–95.

Firsching F. H. and Kell J. C. (1993) The solubility of the rare-earth-metal phosphates in seawater. *J. Chem. Eng. Data* **38**, 132–133.

Foley N. K., Ayusor A., Bern C. R., Hubbard B. E. and Vazquez J. A. (2014) REE distribution and mobility in regolith formed on granite bedrock of the southeast United States. *Acta Geol. Sin.* **88**, 428–430.

Förster H. J. (1998) The chemical composition of REE-Y-Th-U-rich accessory minerals in peraluminous granites of the Erzgebirge-Fichtelgebirge region, Germany, Part I: The monazite-(Ce)-brabantite solid solution series. *Am. Mineral.* **83**, 259–272.

Gausse C., Szenknect S., Qin D. W., Mesbah A., Clavier N., Neumeier S., Bosbach D. and Dacheux N. (2016) Determination of the solubility of rhabdophanes $LnPO_4 \cdot 0.667H_2O$ (Ln = La to Dy). *Eur. J. Inorg. Chem.* 4615–4630.

Gavrichev K. S., Ryumin M. A., Tyurin A. V., Gurevich V. M. and Komissarova L. N. (2009) The heat capacity and thermodynamic functions of $EuPO_4$ over the temperature range 0–1600 K. *Russ. J. Phys. Chem. A* **83**, 901–906.

Gavrichev K. S., Gurevich V. M., Ryumin M. A., Tyrin A. V. and Komissarova L. N. (2016) Low-temperature heat capacity and thermodynamic properties of $PrPO_4$. *Geochemistry Int.* **54**, 362–368.

Geisler T., Popa K. and Konings R. J. M. (2016) Evidence for lattice strain and non-ideal behavior in the $(La_{1-x}Eu_x)PO_4$ Solid Solution from X-ray diffraction and vibrational spectroscopy. *Front. Earth Sci.* **4**, 1–12.

Gratz R. and Heinrich W. (1997) Monazite-xenotime thermobarometry: Experimental calibration of the miscibility gap in the binary system $CePO_4$-YPO_4. *Am. Mineral.* **82**, 772–780.

Gysi A. P., Harlov D. and Miron G. D. (2015) The solubility of xenotime-(Y) and other HREE phosphates ($DyPO_4$, $ErPO_4$, and $YbPO_4$) in aqueous solutions from 100 to 250 °C and p_{sat}. *Chem. Geol.* **401**, 83–95.

Gysi A. P., Harlov D. and Miron G. D. (2018) The solubility of monazite ($CePO_4$), $SmPO_4$, and $GdPO_4$ in aqueous solutions from 100 to 250 °C. *Geochim. Cosmochim. Acta* **242**, 143–164.

Haas J. R., Shock E. L. and Sassani D. C. (1995) Rare earth elements in hydrothermal systems: Estimates of standard partial molal thermodynamic properties of aqueous complexes of the rare earth elements at high pressures and temperatures. *Geochim. Cosmochim. Acta* **59**, 4329–4350.

Harlov D. E., Andersson U. B., Förster H. J., Nyström J. O., Dulski P. and Broman C. (2002) Apatite-monazite relations in the Kiirunavaara magnetite-apatite ore, northern Sweden. *Chem. Geol.* **191**, 47–72.

Harlov D. E., Meighan C. J., Kerr I. D. and Samson I. M. (2016) Mineralogy, chemistry, and fluid-aided evolution of the Pea Ridge Fe oxide-(Y+REE) deposit, Southeast Missouri, USA. *Econ. Geol.* **111**, 1963–1984.

Harrison T. M., Catlos E. J. and Montel J. M. (2002) U-Th-Pb dating of phosphate minerals. *Rev. Mineral. Geochemistry* **48**, 524–558.

Heinrich W., Andrehs G. and Franz G. (1997) Monazite-xenotime miscibility gap thermometry. I. An empirical calibration. *J. Metamorph. Geol.* **15**, 3–16.

Helgeson H. C. and Kirkham D. H. (1974) Theoretical prediction of the thermodynamic behavior of aqueous electrolytes at high pressures and temperatures: II, Debye-Hückel parameters for activity coefficients and relative partial molal properties. *Am. J. Sci.* **274**, 1199–1261.

Helgeson H. C., Kirkham D. H. and Flowers G. C. (1981) Theoretical prediction of the thermodynamic behavior of aqueous electrolytes at high pressures and temperatures: IV. Calculation of activity coefficients, osmotic coefficients, and apparent molal and standard and relative partial molal properties to 600 °C. *Am. J. Sci.* **281**, 1249–1516.

Hetherington C. J., Harlov D. E. and Budzyń B. (2010) Experimental metasomatism of monazite and xenotime: mineral stability, REE mobility and fluid composition. *Mineral. Petrol.* **99**, 165–184.

Hirsch A., Kegler P., Alencar I., Ruiz-Fuertes J., Shelyug A., Peters L., Schreinemachers C., Neumann A., Neumeier S., Liermann H. P., Navrotsky A. and Roth G. (2017) Structural, vibrational, and thermochemical properties of the monazite-type solid solution $La_{1-x}Pr_xPO_4$. *J. Solid State Chem.* **245**, 82–88.

Huittinen N., Arinicheva Y., Kowalski P. M., Vinograd V. L., Neumeier S. and Bosbach D. (2017) Probing structural homogeneity of $La_{1-x}Gd_xPO_4$ monazite-type solid solutions by combined spectroscopic and computational studies. *J. Nucl. Mater.* **486**, 148–157.

Janots E., Brunet F., Goffé B., Poinssot C., Burchard M. and Cemič L. (2007) Thermochemistry of monazite-(La) and dissakisite-(La): implications for monazite and allanite stability in metapelites. *Contrib. to Mineral. Petrol.* **154**, 1–14.

Jonasson R. G., Bancroft G. M. and Nesbitt H. W. (1985) Solubilities of some hydrous REE phosphates with implications for diagenesis and sea water concentrations. *Geochim. Cosmochim. Acta* **49**, 2133–2139.

Kestin J., Sengers J. V., Kamgar-Parsi B. and Levelt Sengers J. M. H. (1984) Thermophysical properties of fluid H_2O. *J. Phys. Chem. Ref. Data* **13**, 175–183.

Kielland J. (1937) Individual activity coefficients of ions in aqueous solutions. *J. Am. Chem. Soc.* **59**, 1675–1678.

Kulik D. A., Wagner T., Dmytrieva S. V., Kosakowski G., Hingerl F. F., Chudnenko K. V. and Berner U. R. (2013) GEM-SELEKTOR geochemical modeling package: revised algorithm and GEMS3K numerical kernel for coupled simulation codes. *Comput. Geosci.* **17**, 1–24.

Li Y., Kowalski P. M., Blanca-Romero A., Vinograd V. and Bosbach D. (2014) Ab initio calculation of excess properties of $La_{1-x}(Ln, An)_xPO_4$ solid solutions. *J. Solid State Chem.* **220**, 137–141.

Li M.Y.H., Zhou M.-F. and Williams-Jones A. E. (2019) The genesis of regolith-hosted heavy rare earth element deposits: Insights from the world class Zudong deposit in Jiangxi Province, South China. *Econ Geol.* **114**, 541–568.

Liu X. and Byrne R. H. (1997) Rare earth and yttrium phosphate solubilities in aqueous solution. *Geochim. Cosmochim. Acta* **61**, 1625–1633.

Mair P., Tropper P., Harlov D. E. and Manning C. E. (2017) The solubility of $CePO_4$ monazite and YPO_4 xenotime in KCl-H_2O fluids at 800 °C and 1.0 GPa: Implications for REE transport in high-grade crustal fluids. *Am. Mineral.* **102**, 2457–2466.

McDonough W. F. and Sun S. (1995) The composition of the Earth. Chem. *Geol.* **120**, 223–253.

Mesmer R. E. and Baes Jr. C. F. (1974) Phosphoric acid dissociation equilibria in aqueous solutions to 300 ºC. *J. Solution Chem.* **3**, 307-322.

Migdisov A. A. and Williams-Jones A. E. (2007) An experimental study of the solubility and speciation of neodymium (III) fluoride in F-bearing aqueous solutions. *Geochim. Cosmochim. Acta* **71**, 3056–3069.

Migdisov A. A., Williams-Jones A. E. and Wagner T. (2009) An experimental study of the solubility and speciation of the Rare Earth Elements (III) in fluoride- and chloride-bearing aqueous solutions at temperatures up to 300 °C. *Geochim. Cosmochim. Acta* **73**, 7087–7109.

Migdisov A. A., Williams-Jones A. E., Brugger J. and Caporuscio F. A. (2016) Hydrothermal transport, deposition, and fractionation of the REE: Experimental data and thermodynamic calculations. *Chem. Geol.* **439**, 13–42.

Montel J. M., Foret S., Veschambre M., Nicollet C. and Provost A. (1996) Electron microprobe dating of monazite. *Chem. Geol.* **131**, 37–53.

Neumeier S., Kegler P., Arinicheva Y., Shelyug A., Kowalski P. M., Schreinemachers C., Navrotsky A. and Bosbach D. (2017) Thermochemistry of $La_{1-x}Ln_xPO_4$-monazites (Ln = Gd, Eu). *J. Chem. Thermodyn.* **105**, 396–403.

Ni Y., Hughes J. M. and Mariano A. N. (1995) Crystal chemistry of the monazite and xenotime structures. *Am. Mineral.* **80**, 21–26.

Poitrasson F., Chenery S. and Bland D. J. (1996) Contrasted monazite hydrothermal alteration mechanisms and their geochemical implications. *Earth Planet. Sci. Lett.* **145**, 79–96.

Poitrasson F., Oelkers E., Schott J. and Montel J. M. (2004) Experimental determination of synthetic $NdPO_4$ monazite end-member solubility in water from 21°C to 300°C: implications for rare earth element mobility in crustal fluids. *Geochim. Cosmochim. Acta* **68**, 2207–2221.

Popa K. and Konings R. J. M. (2006) High-temperature heat capacities of $EuPO_4$ and $SmPO_4$ synthetic monazites. *Thermochim. Acta* **445**, 49–52.

Popa K., Jutier F., Wastin F. and Konings R. J. M. (2006) The heat capacity of $NdPO_4$. *J. Chem. Thermodyn.* **38**, 1306–1311.

Popa K., Konings R. J. M. and Geisler T. (2007) High-temperature calorimetry of $(La_{1-x}Ln_x)PO_4$ solid solutions. *J. Chem. Thermodyn.* **39**, 236–239.

Pourtier E., Devidal J. L. and Gibert F. (2010) Solubility measurements of synthetic neodymium monazite as a function of temperature at 2 kbars, and aqueous neodymium speciation in equilibrium with monazite. *Geochim. Cosmochim. Acta* **74**, 1872–1891.

Pyle J. M., Spear F. S., Rudnick R. L. and McDonough W. F. (2001) Monazite-xenotime-garnet equilibrium in metapelites and a new monazite-garnet thermometer. *J. Petrol.* **42**, 2083–2107.

Rasmussen B., Fletcher I. R., Muhling J. R., Gregory C. J. and Wilde S. A. (2011) Metamorphic replacement of mineral inclusions in detrital zircon from Jack Hills, Australia: Implications for the Hadean Earth. *Geology* **39**, 1143–1146.

Robinson R. A. and Stokes R. H. (1959) *Electrolyte Solutions*. Butterworth, London.

Rudolph W. W. (2012) Raman-spectroscopic measurements of the first dissociation constant of aqueous phosphoric acid solution from 5 to 301 ºC. *J. Solution Chem.* **41**, 630-645.

Schaltegger U., Pettke T., Audétat A., Reusser E. and Heinrich C. A. (2005) Magmatic-to-hydrothermal crystallization in the W-Sn mineralized Mole Granite (NSW, Australia). Part I: Crystalllization of zircon and REE-phosphates over three million years - a geochemical and U-Pb geochronological study. *Chem. Geol.* **220**, 215–235.

Schmidt C., Rickers K., Bilderback D. H. and Huang R. (2007) In situ synchrotron-radiation XRF study of REE phosphate dissolution in aqueous fluids to 800 °C. *Lithos* **95**, 87–102.

Seydoux-Guillaume A. M., Paquette J. L., Wiedenbeck M., Montel J. M. and Heinrich W. (2002) Experimental resetting of the U-Th-Pb systems in monazite. *Chem. Geol.* **191**, 165–181.

Shannon R.D. (1976) Revised eff ective ionic radii and systematic studies of interatomic distances in halides and chalcogenides. *Acta Crystallographica* **Section A 32**, 751–767.

Shelyug A., Mesbah A., Szenknect S., Clavier N., Dacheux N. and Navrotsky A. (2018) Thermodynamics and stability of rhabdophanes, hydrated rare earth phosphates $REPO_4 \cdot n\ H_2O$. *Front. Chem.* **6**, 604.

Shock E. L. and Helgeson H. C. (1988) Calculation of the thermodynamic and transport properties of aqueous species at high pressures and temperatures: Correlation algorithms for ionic species and equation of state predictions to 5 kb and 1000°C. *Geochim. Cosmochim. Acta* **52**, 2009–2036.

Shock E. L., Helgeson H. C. and Sverjensky D. A. (1989) Calculation of the thermodynamic and transport properties of aqueous species at high pressures and temperatures: Standard partial molal properties of inorganic neutral species. *Geochim. Cosmochim. Acta* **53**, 2157–2183.

Shock E. L., Oelkers E. H., Johnson J. W., Sverjensky D. A. and Helgeson H. C. (1992) Calculation of the thermodynamic properties of aqueous species at high pressures and temperatures. Effective electrostatic radii, dissociation constants and standard partial molal properties to 1000 °C and 5 kbar. *J. Chem. Soc. Farady Trans.* **88**, 803–826.

Shock E. L., Sassani D. C., Willis M. and Sverjensky D. A. (1997) Inorganic species in geologic fluids: Correlations among standard molal thermodynamic properties of aqueous ions and hydroxide complexes. *Geochim. Cosmochim. Acta* **61**, 907–950.

Smith M. P., Henderson P. and Peishan Z. (1999) Reaction relationships in the Bayan Obo Fe-REE-Nb deposit Inner Mongolia, China: implications for the relative stability of rare-earth element phosphates and fluorocarbonates. *Contrib. to Mineral. Petrol.* **134**, 294–310.

Smith M. P., Henderson P. and Campbell L. S. (2000) Fractionation of the REE during hydrothermal processes: constraints from the Bayan Obo Fe-REE-Nb deposit, Inner Mongolia, China. *Geochim. Cosmochim. Acta* **64**, 3141–3160.

Smith M. P., Moore K., Kavecsánszki D., Finch A. A., Kynicky J. and Wall F. (2016) From mantle to critical zone: A review of large and giant sized deposits of the rare earth elements. *Geosci. Front.* **7**, 315–334.

Spear F. S. and Pyle J. M. (2002) Apatite, monazite, and xenotime in metamorphic rocks. *Rev. Mineral. Geochemistry* **48**, 293–335.

Tanger J. C. and Helgeson H. C. (1988) Calculation of the thermodynamic and transport properties of aqueous species at high pressures and temperatures: revised equations of state for the standard partial molal properties of ions and electrolytes. *Am. J. Sci.* **288**, 19–98.

Teufel S. and Heinrich W. (1997) Partial resetting of the U-Pb isotope system in monazite through hydrothermal experiments: An SEM and U-Pb isotope study. *Chem. Geol.* **137**, 273–281.

Thiriet C., Konings R. J. M., Javorský P., Magnani N. and Wastin F. (2005) The low temperature heat capacity of $LaPO_4$ and $GdPO_4$, the thermodynamic functions of the monazite-type $LnPO_4$ series. *J. Chem. Thermodyn.* **37**, 131–139.

Thust A., Arinicheva Y., Haussühl E., Ruiz-Fuertes J., Bayarjargal L., Vogel S. C., Neumeier S. and Winkler B. (2015) Physical properties of $La_{1-x}Eu_xPO_4$, $0 \leq x \leq 1$, monazite-type ceramics. *J. Am. Ceram. Soc.* **98**, 4016–4021.

Tropper P., Manning C. E. and Harlov D. E. (2011) Solubility of $CePO_4$ monazite and YPO_4 xenotime in H_2O and H_2O-NaCl at 800 °C and 1 GPa: Implications for REE and Y transport during high-grade metamorphism. *Chem. Geol.* **282**, 58–66.

Ushakov S. V., Helean K. B., Navrotsky A. and Boatner L. A. (2001) Thermochemistry of rare-earth orthophosphates. *J. Mater. Res.* **16**, 2623–2633.

Wagner T., Kulik D. A., Hingerl F. F. and Dmytrieva S. V. (2012) GEM-SELEKTOR geochemical modeling package: TSolMod library and data interface for multicomponent phase models. *Can. Mineral.* **50**, 1173–1195.

Williams M. L., Jercinovic M. J., Harlov D. E., Budzyń B. and Hetherington C. J. (2011) Resetting monazite ages during fluid-related alteration. *Chem. Geol.* **283**, 218–225.

Wood S. A., Palmer D. A., Wesolowski D. J. and Benezeth P. (2002) The aqueous geochemistry of the rare earth elements and yttrium. Part XI. The solubility of $Nd(OH)_3$ and hydrolysis of Nd^{3+} from 30 to 290 ^oC at saturated water vapor pressure with in-situ pH_m measurement. *Geochemical Soc. Spec. Publ.* 229–256.

Xu C., Kynický J., Smith M. P., Kopriva A., Brtnický M., Urubek T., Yang Y., Zhao Z., He C. and Song W. (2017) Origin of heavy rare earth mineralization in South China. *Nat. Commun.* **8**.

Table all

Table 1. Mean values of the logarithm of the solubility products (K_{s0}) and standard deviations of the mean (1σ) for measured monazite endmembers between 100 and 250 °C at *swvp*. Values in parentheses are the number of replicate experiments used to evaluate the experimental uncertainty. Experimental data are listed in Appendix A.

Temp.	$LaPO_4$		$PrPO_4$		$NdPO_4$		$EuPO_4$	
(°C)	logK_{s0}	1σ	logK_{s0}	1σ	logK_{s0}	1σ	logK_{s0}	1σ
100	-27.97(3)	±0.11	-28.03(4)	±0.18	-28.07(5)	±0.20	-27.67(3)	±0.23
150	-28.79(2)	±0.01	-29.01(3)	±0.18	-28.95(3)	±0.26	-28.53(2)	±0.05
200	-30.19(3)	±0.11	-30.36(2)	±0.01	-30.59(3)	±0.08	-30.21(2)	±0.40
250	-32.07(4)	±0.16	-31.97(2)	±0.06	-32.33(2)	±0.29	-32.08(2)	±0.01

Table 2. Empirical coefficients retrieved by regression of the experimental values listed in Table 1 for the temperature (in Kelvin) dependence of the logarithm of the solubility products (K_{s0}) of monazite endmembers. Three fits were evaluated including an unconstrained fit (Fit 1) and two constrained fits, where either $\Delta_f H^0$ was fixed and S^0 calculated (Fit 2) or $\Delta_f H^0$ was calculated and S^0 fixed (Fit 3). Thermodynamic relationships are given in Appendix D.

	logK_{s0} = A + BT + C/T + Dlog(T)				R^2	logK_{s0}	$\Delta_f H^0_{Tr,Pr}$	$S^0_{Tr,Pr}$
	A	B	C	D		(25 °C, 1 bar)	kJ mol^{-1}	J mol^{-1} K^{-1}
Fit 1, unconstrained								
$LaPO_4$	24.73	-7.471E-02	-9.261E+03	-	0.996	-28.60	-	-
$PrPO_4$	7.00	-5.443E-02	-5.490E+03	-	0.993	-27.63	-	-
$NdPO_4$	18.60	-6.883E-02	-7.827E+03	-	0.986	-28.16	-	-
$EuPO_4$	24.20	-7.518E-02	-8.881E+03	-	0.989	-28.01	-	-
Fit 2, $\Delta_f H^0$ optimized, S° calculated								
$LaPO_4$	-904.63	-2.452E-01	2.449E+04	3.509E+02	0.996	-27.18	-1970.7[a]	137.1
$PrPO_4$	-379.76	-1.260E-01	8.469E+03	1.462E+02	0.993	-27.11	-1969.5[a]	135.4
$NdPO_4$	-493.68	-1.618E-01	1.092E+04	1.931E+02	0.985	-27.42	-1968.4[a]	114.0
$EuPO_4$	-717.78	-2.106E-01	1.817E+04	2.800E+02	0.988	-26.98	-1870.6[a]	112.0
Fit 3, S^0 optimized, $\Delta_f H^0$ calculated								
$LaPO_4$	-769.46	-2.205E-01	1.957E+04	2.999E+02	0.996	-27.33	-1980.5	108.2[b]
$PrPO_4$	-352.57	-1.209E-01	7.500E+03	1.359E+02	0.993	-27.17	-1971.2	130.3[c]
$NdPO_4$	-539.30	-1.703E-01	1.255E+04	2.104E+02	0.985	-27.22	-1965.4	122.9[d]
$EuPO_4$	-744.65	-2.157E-01	1.912E+04	2.902E+02	0.988	-26.96	-1868.9	117.1[e]

[a]Ushakov et al. (2001), [b]Thiriet et al. (2005), [c]Gavrichev et al. (2016), [d]Popa et al. (2006), and [e]Gavrichev et al. (2009).

Table 3. Thermodynamic properties of monazite endmembers at reference conditions (1 bar and 25 °C) derived in this study (in italics) and from calorimetric measurements. Values in bold are recommended for modeling the solubility of monazite in hydrothermal aqueous solutions.

	$\Delta_f G^0_{Tr,Pr}$ kJ mol^{-1}	$\Delta_f H^0_{Tr,Pr}$ kJ mol^{-1}	S^0_{Tr} J mol^{-1} K^{-1}	V_m J bar^{-1}	$C_P°$ J mol^{-1} K^{-1}	$C_P^0 = a + bT + c/T^2$ J mol^{-1} K^{-1}			T Range (K)
						a	b x 10^3	c x 10^{-6}	
$LaPO_4$	***-1861.2***	***-1980.5***	**108.24**[a]	**4.603**[b]	**101.28**[a]	**121.1275**[k]	**30.1156**[k]	**-2.5625**[k]	300-1570[k]
	-1850.5[a,c]	-1970.7 ± 1.8[c]	106.3[d]	4.617[a]	100.8[d]	102.96[e]	53[e]	-1.4322[e]	143-723[e]
	-1865.9[e]	-1985.7 ± 3.0[e]	104.9 ± 1.6[e]	4.601[c]	102.1[e]				
		-1994.36 ± 2.68[f]		4.621[f]	101.7[g]				
		-1994.26 ± 4.25[h]							
$PrPO_4$	***-1855.6***	***-1971.2***	**130.25**[i]	**4.445**[b]	**105.60** ± 0.03[i]	**124.4998**[k]	**30.3743**[k]	**-2.4495**[k]	300-1570[k]
	-1850.5[c,i]	-1969.5 ± 3.7[c]		4.463[c]					
		-1979.84 ± 6.86[h]		4.484[i]					
$NdPO_4$	***-1846.2***	***-1965.4***	**122.9**[j]	**4.386**[b]	**104.8**[j]	**132.9631**[k]	**22.5413**[k]	**-3.1009**[k]	300-1570[k]
	-1849.6[c,j]	-1968.4 ± 2.3[c]		4.398[c]					
$EuPO_4$	***-1746.0***	***-1868.9***	**117.06** ± 0.15[l]	**4.240**[b]	**113.05** ± 0.09[l]	**137.5600**[k]	**17.6934**[k]	**-2.7854**[k]	300-1570[k]
	-1747.8[c,l]	-1870.6 ± 2.6[c]		4.248[c]	110.2[g]				
		-1870.70 ± 3.32[f]		4.254[f]	111.5[k]				

[a]Thiriet et al. (2005), [b]Ni et al. (1995), [c]Ushakov et al. (2001), [d]Bauer et al. (2016), [e]Janots et al. (2017), [f]Neumeier et al. (2017), [g]Thust et al. (2015), [h]Hirsch et al. (2017), [i]Gavrichev et al. (2016), [j]Popa et al. (2016), [k]Popa and Konings (2006), [l]Gavrichev et al. (2009).

All figures+fig captions

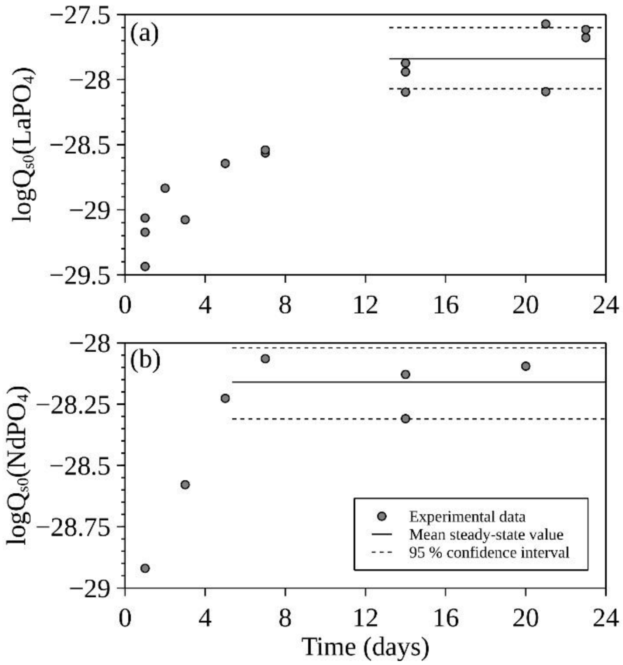

Fig 1. Kinetic plots showing the logarithm of the reaction quotient (Q_{s0}) as a function of time (in days) for the solubility of (a) $LaPO_4$ and (b) $NdPO_4$ at 100 ºC and *swvp*. Steady-state concentrations in the experiments were reached within 5–14 days.

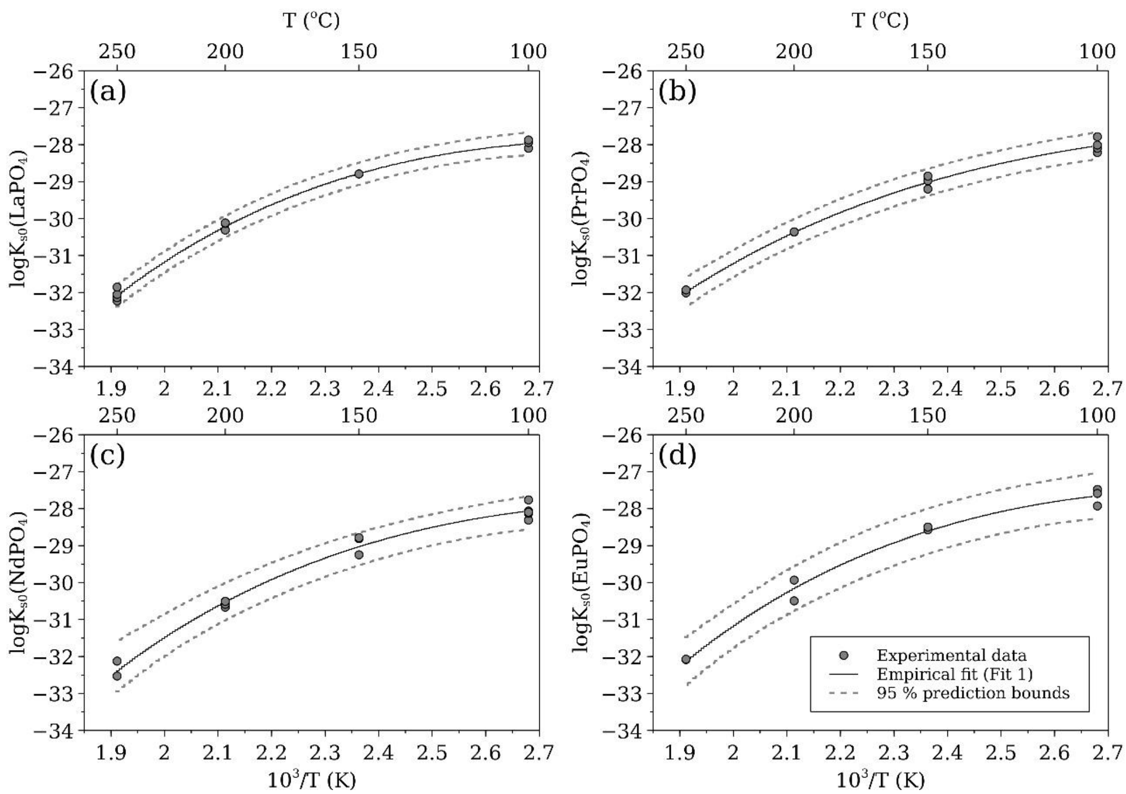

Fig 2. Logarithm of the solubility products (K_{s0}) of monazite endmembers as a function of inverse temperature (10^3/T, in Kelvin) between 100 and 250 °C at *swvp*. Experimental data are listed in Table 1 and Appendix A. Solid black lines are the non-linear regressions using Eq. 13 (Fit 1, Table 2), and the gray dotted lines are their prediction bounds at the 95% confidence.

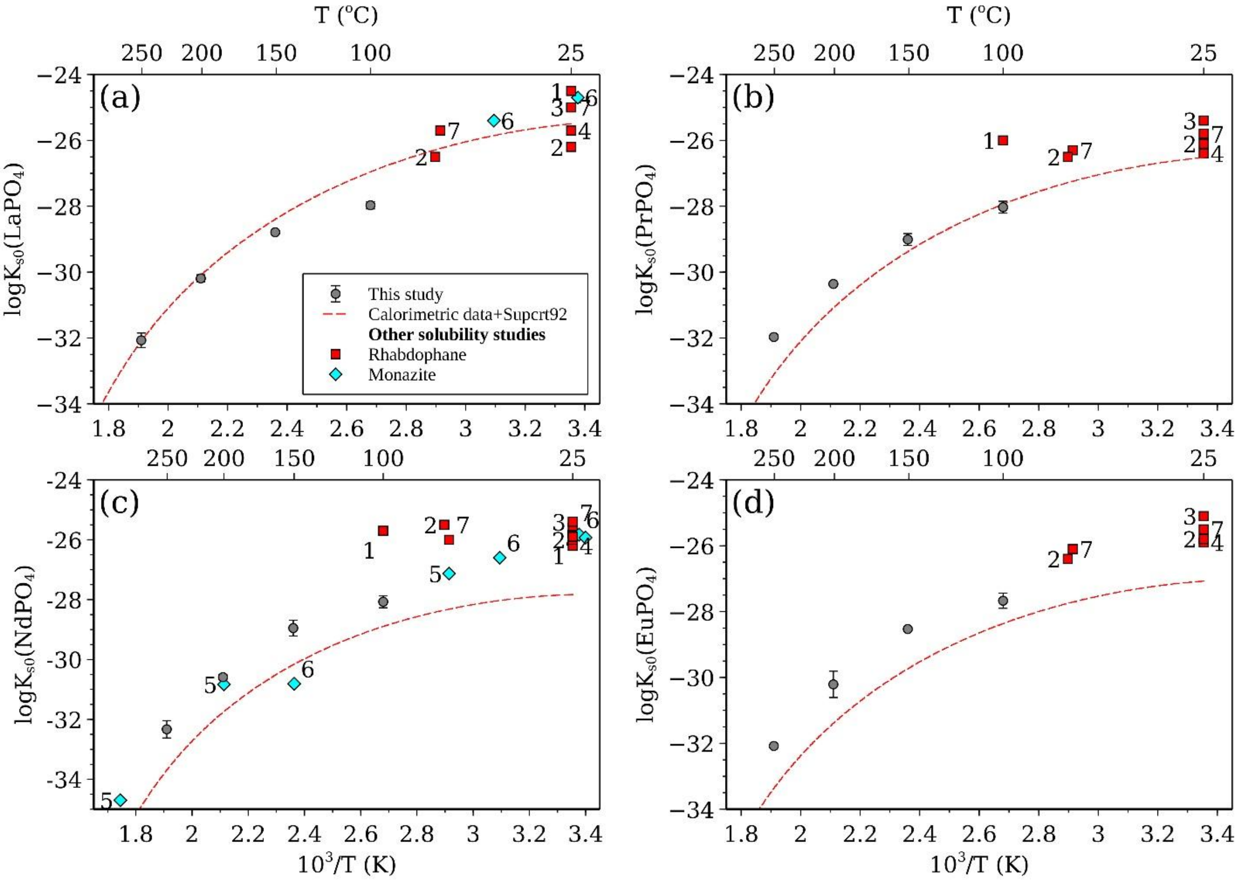

Fig 3. Comparison of the logarithm of the solubility products (K_{s0}) of monazite endmembers as a function of inverse temperature (10^3/T, in Kelvin) between 100 and 250 °C at *swvp* (Table 1). Also shown are the results from other solubility studies: (1) Jonasson et al. (1985), (2) Firsching and Brune (1991), (3) Byrne and Kim (1993),jpg) Liu and Byrne (1997), (5) Poitrasson et al. (2004), (6) Cetiner et al. (2005), and (7) Gausse et al. (2016). The red curve corresponds to the calculated logK_{s0} values from the calorimetric data of monazite (Table 3) combined with the thermodynamic data of aqueous species from Supcrt92 (Appendix C).

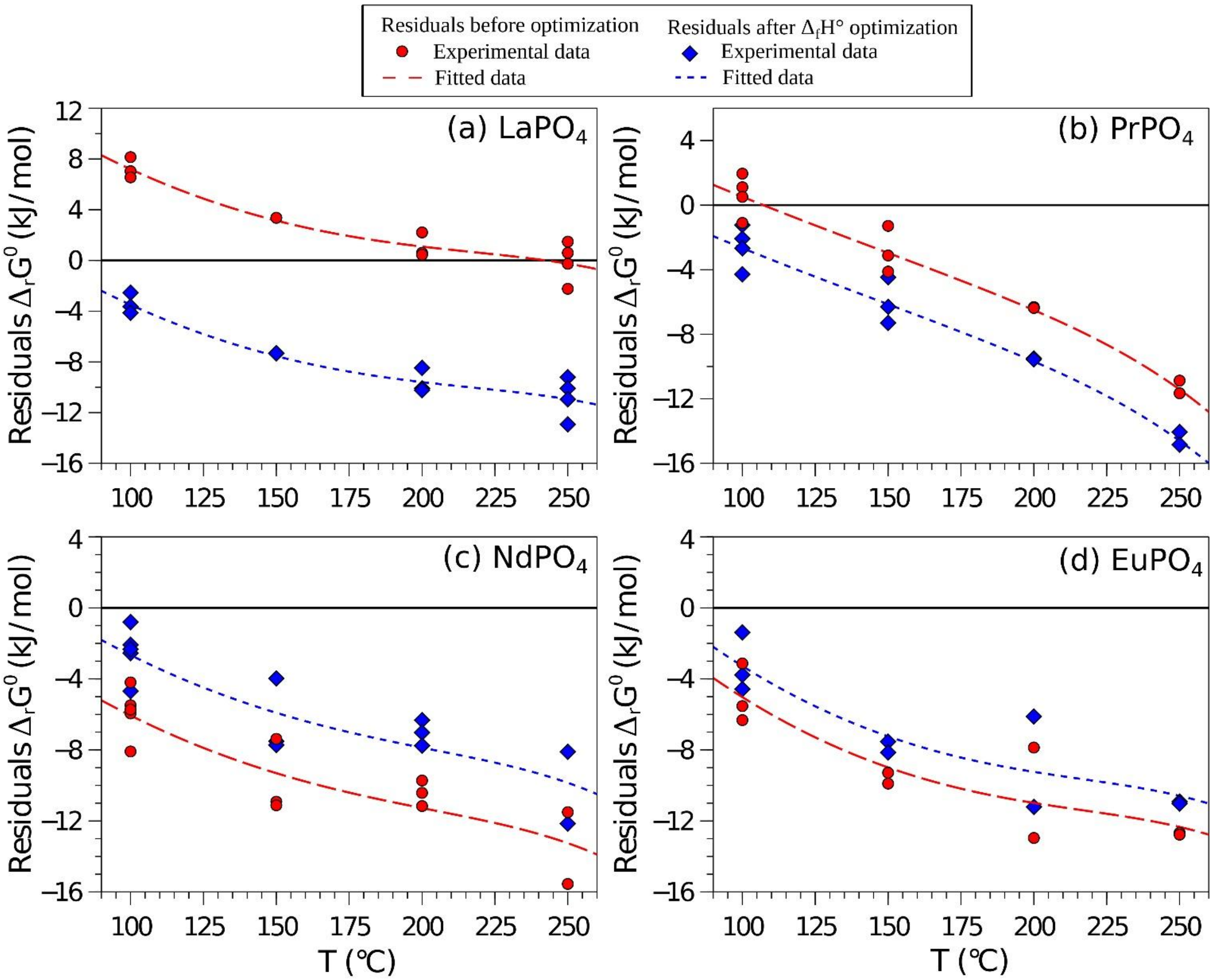

Fig 4. Residuals standard Gibbs energy of reaction (Δ_rG^0) before (red lines) and after (blue lines) optimization of Δ_fH^0 values of monazite. The residuals represent the difference between the experimental fits and calculated values from calorimetric data of monazite (Table 3) combined with the properties of aqueous species from Supcrt92 (Appendix C). The symbols show the residuals of the measured experimental solubility data.

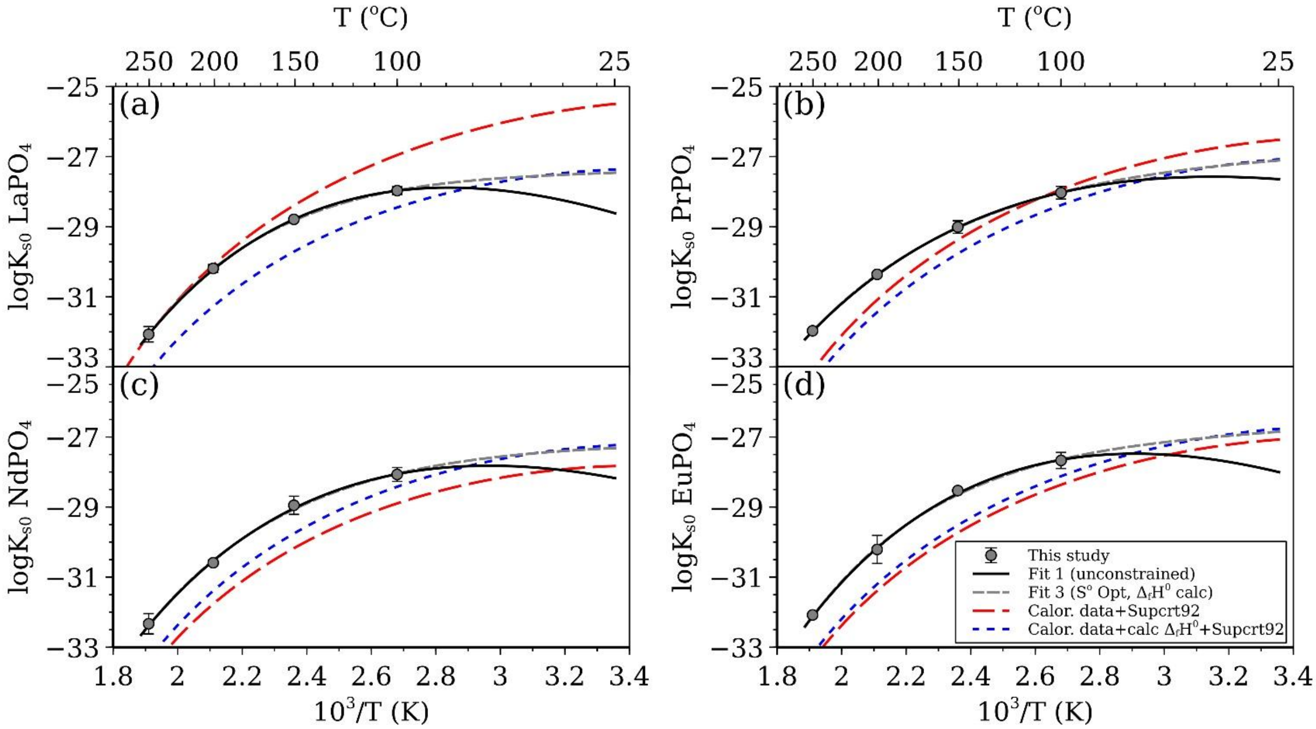

Fig 5. Comparison of the logarithm of the solubility products (logK_{s0}) of monazite endmembers as a function of inverse temperature (10^3/T, in Kelvin) showing the unconstrained fit (Fit 1, Table 2) and the optimized fits (Fit 3, Table 2) used to retrieve a new $\Delta_f H^0_{Tr,Pr}$ value for monazite. The blue curves correspond to the calculated solubilities using the new $\Delta_f H^0_{Tr,Pr}$ values for monazite retrieved in this study (Table 3). The red curves correspond to the calculated solubilities from the calorimetric data of monazite (Table 3) combined with the thermodynamic data of aqueous species from Supcrt92 (Appendix C).

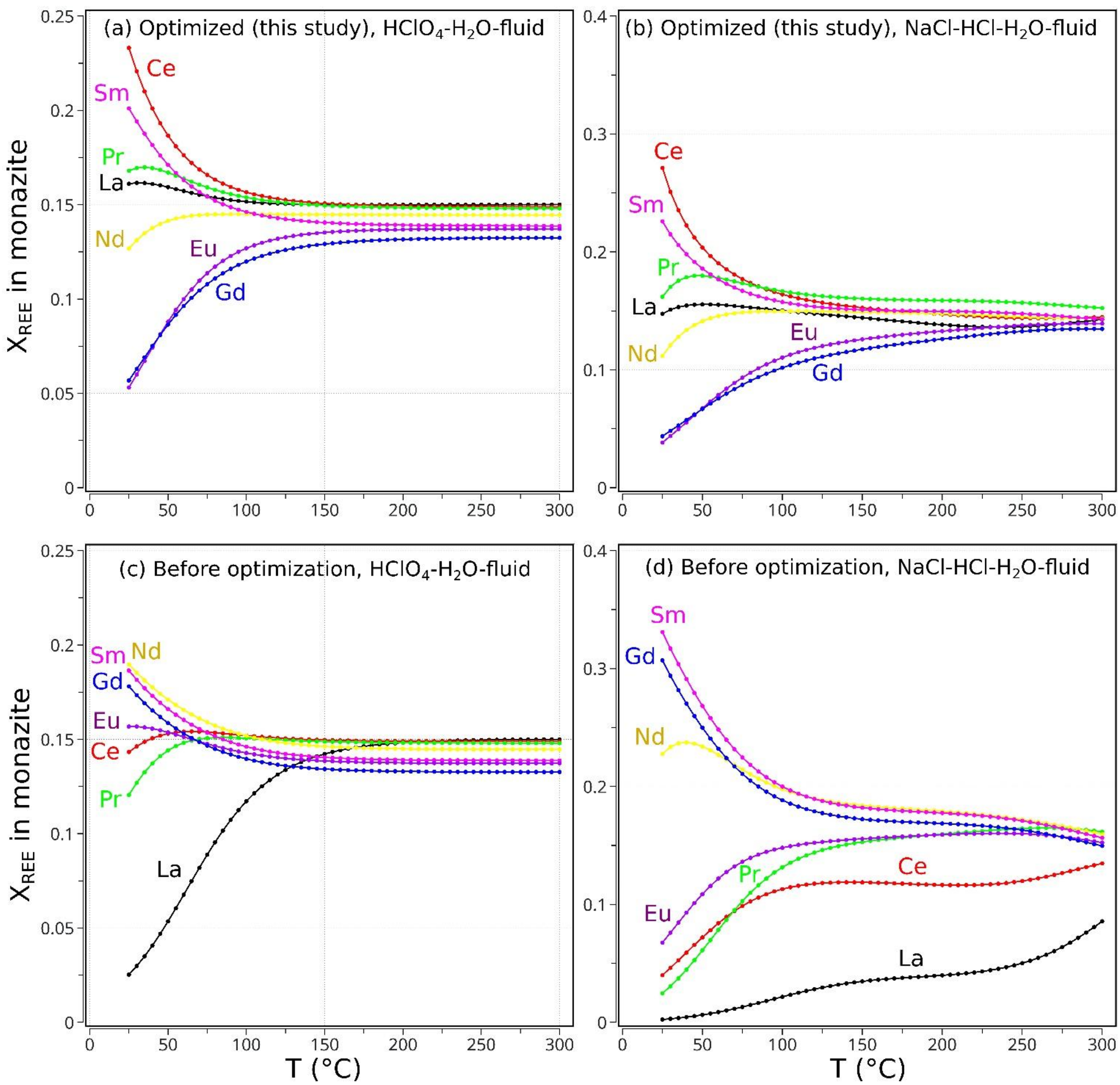

Fig 6. Simulated REE composition (X, mole fraction) of an ideal monazite solid solution in equilibrium with 1000 g of an acidic hydrothermal fluid (pH of 2, 5 ppm P, and 1 ppm of each REE) cooled from 300 to 25 °C at saturated water vapor pressure. (a-b) Simulations using the optimized enthalpy data for monazite derived from the solubility experiments (Table 3) and from Gysi et al. (2018), and (c-d) from combining previous literature data for monazite with Supcrt92. Two initial fluid compositions were reacted with 1 g of leucogranite (35 wt.% quartz, 29 wt.% albite, 17 wt.% microcline, and 19 wt.% muscovite), consisting of either perchloric acid (a,c: $HClO_4$-H_2O-fluid) or hydrochloric acid and 10 wt.% NaCl (b,d: NaCl-HCl-H_2O-fluid), to test the effects of aqueous REE chloride complex formation on the model.

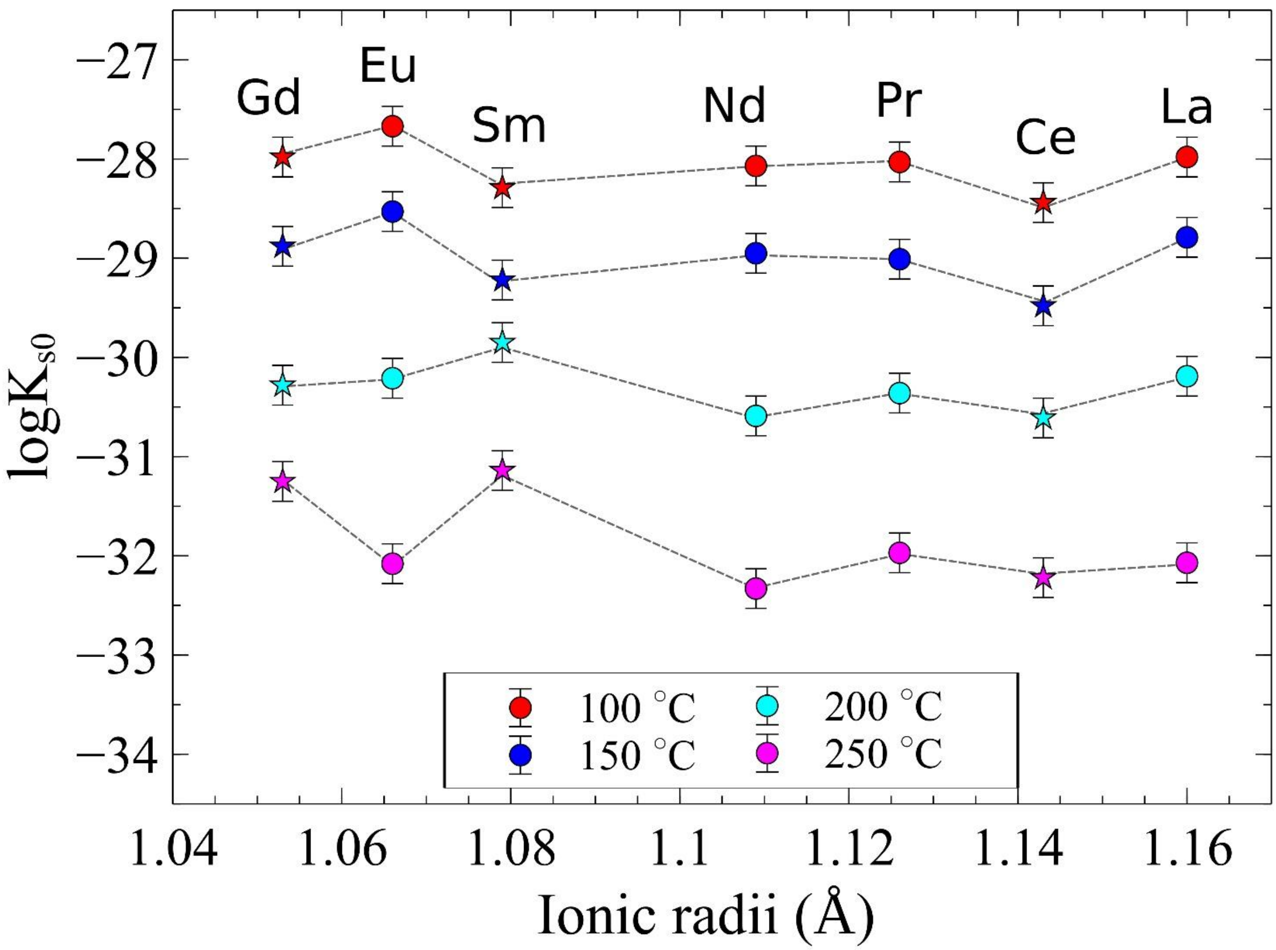

Fig 7**.** Comparison of the solubility products (K_{s0}) of monazite as a function of temperature and ionic radii of the REE in 8-fold coordination (Shannon, 1976). Star symbols are from the study of Gysi et al. (2018) showing the measured solubilities of $CePO_4$, $SmPO_4$, and $GdPO_4$.

Research Data

Click here to download Electronic Annex: Supplementary_Tables.xlsx

Appendix A-D

Click here to download Appendix: Appendix_Compiled-AG.docx